

Simulation of Spot Melting Scan Strategy to Predict Columnar to Equiaxed Transition in Metal Additive Manufacturing

Y.S. Lee^{a, b}, M.M. Kirka^{a, b}, N. Raghavan^c and R.R. Dehoff^{a, b}

a. Manufacturing Demonstration Facility, Oak Ridge National Laboratory, Knoxville, TN, USA

b. Materials Science and Technology Division, Oak Ridge National Laboratory, Oak Ridge, TN, USA

c. Department of Mechanical, Aerospace and Biomedical Engineering, University of Tennessee, Knoxville, TN, USA

Abstract

Recently, additive manufacturing (AM) processes are transforming from rapid prototyping technology to mass industrial production due to increase in the fidelity of the AM machines. This trend triggers the process optimization for various applications. In prior literature, high-fidelity numerical models have been presented to understand the rapid solidification conditions occurring during the process which includes heat transfer, fluid flow and beam interaction with the raw material. However, most of these models are simulating few melt passes and it is computationally expensive to simulate an entire layer of the component being fabricated. In this study, we use a low-fidelity model to simulate an entire layer. We also introduce a new melt strategy to control the solidification microstructure (i.e. columnar to equiaxed transition). The response of the solidification morphology to process parameters (ex. point offset, power, spot time) are investigated in terms of thermal gradient G and solidification rate R . The model is validated with the experimental microstructure data.

1. Introduction

On-demand control of the local microstructure has been unachievable (or hardly achievable) before the advent of additive manufacturing (AM) technology. It is because heat transfer control at microscale was almost impossible in the traditional manufacturing technologies. Recent progress in AM technologies has triggered wider interest in achieving the control of solidification microstructure. The capability of controlling microstructure in electron beam melting (EBM) has been demonstrated in the recent studies [1, 2].

Solidification values of thermal gradient (G) and solidification rate (R) can be used as a pointer to determine the solidification morphology [2-5]- i.e. Columnar to Equiaxed Transition (CET). The behavior of G and R can be determined by transient thermal characteristics of the process. Hence, understanding the transient heat transfer characteristic as a function of process

parameters, scan strategy, and part geometry is important to control the microstructure. However, owing to a transient and local feature of AM, obtaining G and R through experiment is highly challenging. In addition, the values can be measured only at the surface of melt pool. Therefore, numerical modeling is preferentially used to obtain a 3-D spatial and temporal information of G and R .

Today's computational capability enables to capture the key features of AM process. Still, the computational cost is expensive for the high-fidelity multi-physics model including temperature dependent properties, fluid mechanics, and heat source-powder particles interaction. It often requires a high performing clusters (HPC) to perform the simulations. Limited access to HPC makes it challenging for a material scientist to simulate the process. The high computational cost limits the simulations to a couple of tracks in the order of millimeters. Existing literature has not extensively discussed the possibility of adopting low-fidelity models for AM simulations [6-10].

Analytical models adopted from welding community have been frequently used in AM to obtain thermal conditions [1, 11]. The absence of numerical iterations in the analytical models reduces the computational cost significantly. However, since it assumes steady-state and semi-infinite boundary conditions, it may not be suitable for a highly transient simulation as well as a simulation requiring an investigation of scan strategy for complex geometries. Low-fidelity model assumes the conduction cooling is dominant over the system. It does not account for latent heat of fusion and phase change and so it does not account for temperature-dependent material properties. Because of those features, although the low-fidelity model sacrifices a certain amount of accuracy, it acquires computational efficiency.

The aim of the present study is to validate the low-fidelity model for the prediction of solidification morphology (i.e. CET) in electron beam melting (EBM). Furthermore, the model is used to provide an insight about the interrelationship between process parameter, build design and microstructure. Finally, the model provides a possible suggestion of process parameters to achieve identical microstructure at the different size of the build.

2. Numerical and Experimental Setup

2.1. Model description

Three-dimensional transient simulation was implemented based on the numerical solution of heat transfer equation using python library codes, FEniCS [12]. The libraries showed realistic and reasonable capability in full description of spot melting pattern having approximately up to 10,000 spots. Fenics is a low-level code for solving partial differential equation (PDE) [13, 14]. Thus, the computational cost is low. The code solves the heat equation using finite element method (FEM) on a predefined mesh. The governing heat conduction equation is given below [13]:

$$\rho C_p \frac{\partial T}{\partial t} = \nabla \cdot (k \nabla T) + \dot{S} \quad (1)$$

where ρ is density of the material, C_p is specific heat, T is temperature, t is time, k is thermal conductivity and \dot{S} is energy input introduced by heat source.

The thermal energy to melt powder particles on the start plate comes from the focused electron beam. A moving volumetric heat source with Gaussian distribution was adopted to consider the material-heat source interaction. The mathematical expression is given below [15]:

$$\dot{S}(x, y, z) = A_e P \frac{2}{\pi r_b^2 d_p} \exp \left\{ -2 \left[\frac{(x^2 + y^2)}{r_b^2} + \left(\frac{z}{d_p} \right)^2 \right] \right\} \quad (2)$$

where A_e is effective absorption coefficient of electron beam, P is electron beam power, r_b is radius of the beam and d_p is the penetration depth, for which 20 μm is used.

2.2. Assumption and boundary conditions

In this work, we made several assumptions to make the simulation tractable. The material properties of IN718 listed in Table 1 are assumed to be constant for all the phases of the material. Material thermal expansion and solidification shrinkage are presumed to be negligible. The effect of fluid flow on temperature distribution and melt pool geometry are not considered due to the limitation of heat transfer calculation.

Table 1 Material properties of IN718 used in simulation

Property	Value	Unit
Density	7451	Kg/m ³
Thermal conductivity	26	W/m-K
Specific heat	600	J/Kg-K
Liquidus Temperature	1610	K
Solidus Temperature	1528	K
Preheat Temperature	1273	K
Emissivity	0.6	-

The geometry and meshes of a prismatic block were created using a built-in Python library in DOLFIN [16]. The domain has dimensions of 20 mm (width) \times 20 mm (length) \times 1 mm (height). The computation domain is spatially discretized into tetrahedral cells. It produced 480K cells. Adiabatic conditions are assumed for the side surfaces since the sides are encapsulated by powder particles.

The conductivity of the powder bed is only 0.3-1.5% of the bulk material [3, 17]. Hence, there is no heat flux passing through the surfaces. Convective heat loss is assumed to be negligible due to vacuum operating condition of EBM. The heat loss by radiation is considered as the equation below:

$$q_{radi} = \varphi \varepsilon (T^4 - T_{vac}^4) \quad (3)$$

where q_{radi} is heat flux by radiation loss, φ is Stefan-Boltzmann constant of $5.67 \times 10^{-8} \text{ W/m}^2$, ε is emissivity and T_{vac} is vacuum temperature.

For systematic investigation of the process parameter and scan strategy effect, twelve simulations were implemented under four categories. First, a constant energy input of 300 J is set for the cases of 1-5 by manipulating power and spot time. The beam power and spot time are fixed at 1200W and 0.25 ms for the cases of 6-8 and 9-11, respectively. Lastly, the point offset (PO) referred as a distance between the neighboring spots and spot time was changed to 0.5 mm and 1 ms. Among the conditions, the cases of 5, 6, 9 and 12 were experimentally performed in a prior publication [18]. Therefore, the four conditions are used to validate this simulation. The conditions used for simulation are listed in Table 2.

Table 2 Process parameters used in simulation

Case	Power (W)	Spot Time (ms)	PO (mm)	Energy (J)	Experiment
1	500	0.6	0.2	300	-
2	600	0.5			-
3	750	0.4			-
4	1000	0.3			-
5	1200	0.25			β -16
6	1200	0.1	0.2	120	β -15
7	1200	0.15		180	-
8	1200	0.2		240	-
9	900	0.25	0.2	225	β -12
10	1050	0.25		262	-
11	1150	0.25		287	-
12	1200	1.0	0.5	1200	γ -16

The scan strategies used for β (PO=0.2mm) and γ (PO=0.5mm) build are schematically illustrated in Fig. 1. The beam begins in the upper left at point 1. The beam makes a jump from 1 to 2 with a fixed spacing. The spacing is determined by the value of PO. Thus, 2 mm and 5 mm spacing is set for β and γ build, respectively. After completing the first row, the beam moves down by a row along Y-axis and starts at the middle of point 1 and 2 in X-coordinate. The third row starts at the same location with the first spot, point 1 in X-coordinate but one row below from the second in Y-coordinate. The detailed description of the filling sequence is presented in the prior literature [18].

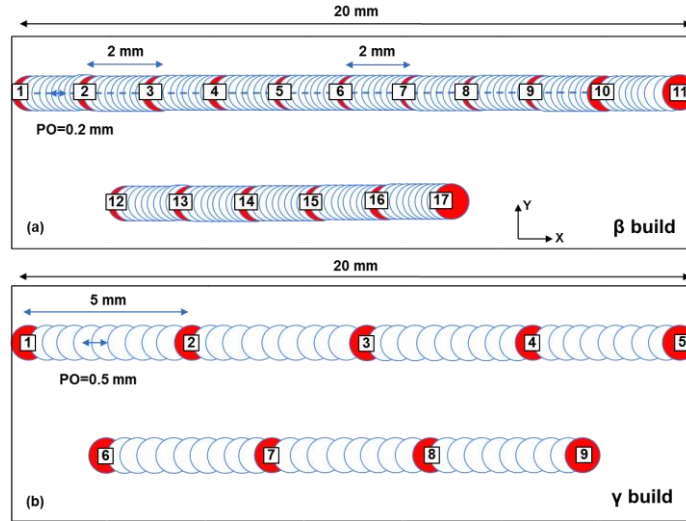


Figure 1 Two scan strategy for β and γ build

2.3. Calculation of thermal gradient and solidification rate

Columnar to Equiaxed Transition (CET) can be determined by solidification values of G and R . The theoretical model to predict CET has been presented in the prior literature [3-5]. The vector \mathbf{G} is normal to the solid-liquid interface of the melt pool. It is composed of three components of G_x , G_y , and G_z . The spatial and temporal value of the components can be obtained from the simulation. Thus, the total thermal gradient \mathbf{G} is calculated by the equation below

$$\mathbf{G} = \sqrt{G_x^2 + G_y^2 + G_z^2} \quad (4)$$

The cooling rate at the solid-liquid interface can be represented by the product of G and R . The values of cooling rate are obtained directly from the simulation. Thus, within the relationship, the solidification rate R can be calculated by the equation below [3]:

$$\text{Solidification Rate (m/s)} = \frac{\text{Cooling Rate (k/s)}}{\text{Thermal Gradient (k/m)}} = \frac{dT/dt}{\sqrt{G_x^2 + G_y^2 + G_z^2}} \quad (5)$$

2.4. Processing of Samples

The modified Arcam S12 machine was employed to fabricate the samples used in this study. 304 stainless steel with dimensions of 150 mm × 150 mm × 10 mm was used as a start plate to fabricate the samples on top of it. The layer thickness of the powder bed used was 50 μm. The accelerating voltage of the electron beam was 60 kV.

3. Results and discussion

3.1. Model Validation

The ability to form either columnar or equiaxed structure was demonstrated in the prior experimental publication of the authors [18]. In the work, the texture upon solidification was controlled through changes in the process parameters associated with spot heat source fill strategies. Figure 2 shows the columnar and equiaxed structure created by using process parameters of case 5 and 12 listed in Table 2. Notice that in Fig. 2(a) individual melt pools are distinctly observed on the top surface of the γ -16 build while a flat surface is found in Fig. 2(b) for the β -16. The columnar and equiaxed structure correspond to the surfaces with individual melt pools (Fig. 2(a)) and flat surface (Fig. 2(b)), respectively. Hence, the feature of melt pool seems to have a strong relationship with the transition of the microstructure. The relationship between melt pool shape, G and R will be further investigated to identify the mechanism of CET in EBM.

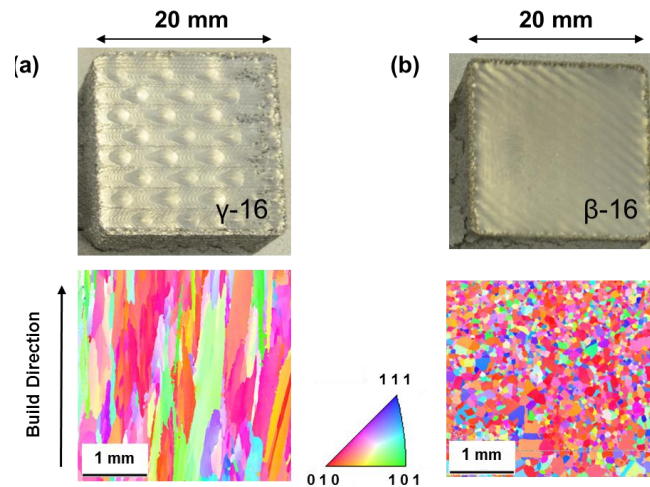


Figure 2 (a) standard melting vs. (b) area melting [3, 18]

The predicted values of G and R for β -12, β -15, β -16 and γ -16 are superimposed on CET curve [1] in Fig. 3. The curve defines the threshold values of G and R such that columnar structure is formed above the green line and equiaxed structure are found below the red line. The middle region is the mixture of columnar and equiaxed structure. The black dots represent averaged values of G and R in each case. In the prior experiment [18], the columnar structure was found in β -12, β -15 γ -16 while equiaxed was in β -16. The prediction matches well with experimentally observed columnar and equiaxed structure.

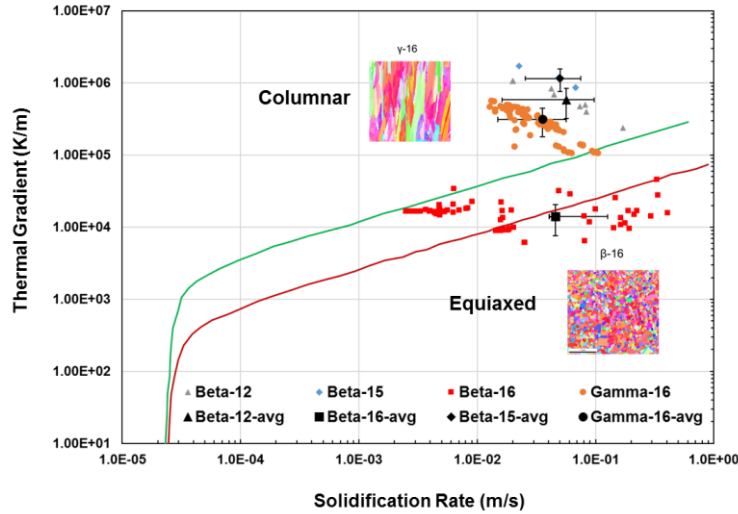


Figure 3 Prediction of solidification morphology compared with experimental results

The temporal evolution of melt pool is shown in Fig. 4 for β -16. In the spot melting strategy, the individual spot melts the powder layer with a skip-distance such that discrete melt pool is formed at a certain distance from the previous spot. As more spots are introduced, the temperature of the layer increases close to solidus temperature. The individual melt pools start to interact with each other and consequently, they merge together. Notice that the band shape melt pool is formed. It is because the spot moves from left to right on the cube and the side walls are surrounded by powder particles. The conductivity of powder bed is 0.3-1.5% of the bulk material [3, 17]. Thus, heat dissipation through the left and right walls remains significantly low. As the spot proceeds more, the band shape melt pool becomes larger and eventually transits to the area melting. A snapshot captured by the infrared camera shown in Fig. 4(i) verifies the band shape of the melt pool in a build using same parameters of spot melting strategy used in simulations.

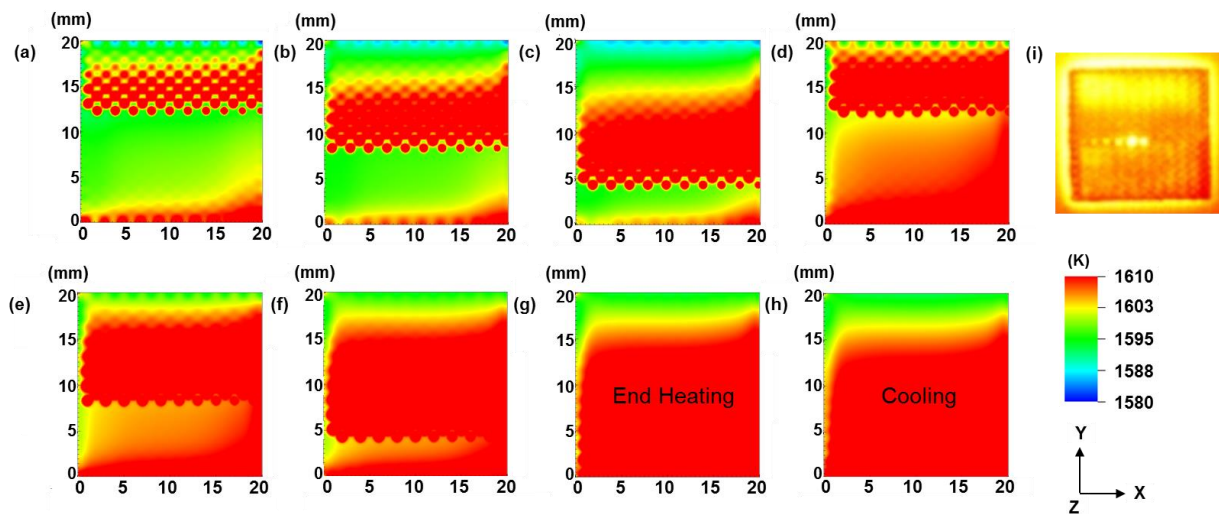


Figure 4 Temporal evolution of melt pool to area melting (β -16): (a) 2.4250s, (b) 2.4375s, (c) 2.4500s, (d) 2.4875s, (e) 2.5000s, (f) 2.5125s, (g) 2.5250s, (h) 2.5375s and (i) Snapshot image by infrared camera that similar with images of (b) and (c)

The predicted cooling rate of samples β -12, β -15, β -16 and γ -16 are presented in Fig. 5. In the same scan strategy, β -16 shows the lowest cooling rate. It is approximately 100 times less than that in β -15. The trend could be explained by the fact that higher energy input at the same geometrical and thermal condition leads to slower heat dissipation through the bottom surface. Notice that the largest value of energy input 1200 J is found in γ -16 that is 4 times larger than the value in β -16. However, the cooling rate in γ -16 is about 8 times faster in β -16. It indicates that scan strategy also influences the cooling trend during the process.

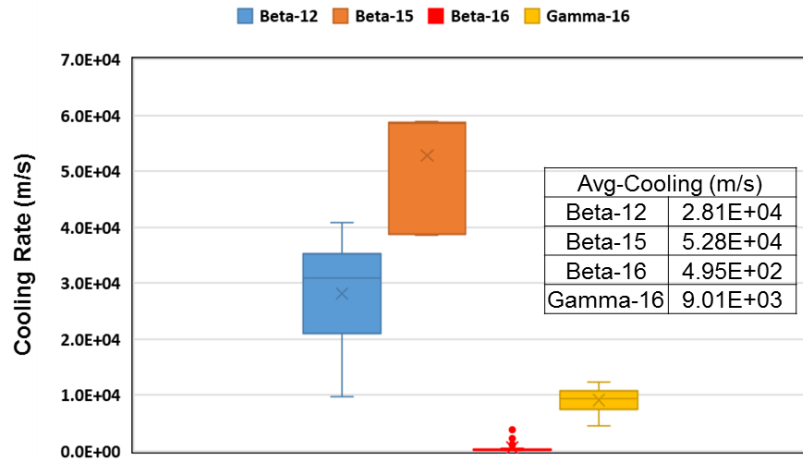


Figure 5 Comparison of cooling rate in the samples of β -12, β -15, β -16 and γ -16, β -16 shows significantly low cooling rate. It is approximately 100 times less than that of β -15.

As seen above, the cooling rate decreases with the increase of the energy input at the same beta scan strategy. However, the value of energy input is not representative of the impact of parameters, i.e. power and spot time, on G and R . Therefore, the individual influence of power or spot time on G and R is investigated by fixing other parameters constant. Figure 6 examines three different powers (900W, 1050W and 1150W) and spot time (0.1 ms, 0.15 ms and 0.2 ms) to understand the influence on CET. Spot time and power are fixed at 0.25 ms in Fig. 6(a) and 1200W in Fig. 6(b), respectively. As the power and spot time increase, the curve falls towards the equiaxed region. Notice that the power was increased by 27 % whereas time was increased by 100%. Relatively larger shift of the curve is found at the power in Fig.6 (a) compared to the curve at the time in Fig.6(b). It indicates that the power has a stronger impact on CET than the time.

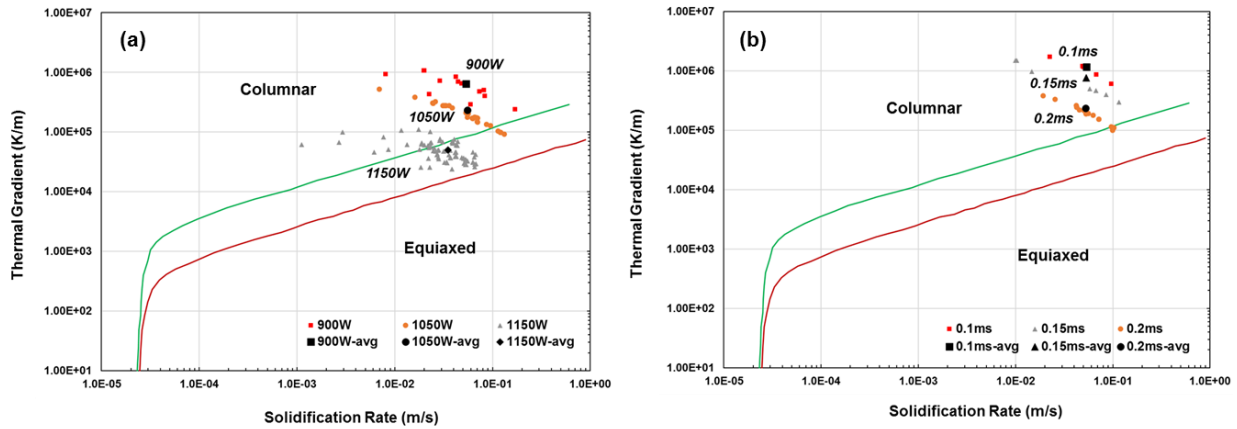


Figure 6 Influence of (a) power and (b) time on transition of solidification morphology

In Fig.7, the effect of the energy on CET is investigated with a fixed energy of 300 J. Four cases of the fixed energy are generated by a combination of power and spot time. To date, most studies on process optimization have used energy density as an only indicator [19]. However, interestingly, the predicted G and R indicate that the same energy does not produce same microstructure. The G and R curve moves towards equiaxed regime with an increase of power but a decrease of time. It is because, unlike general raster scan strategy, the spot goes to the end-corner of the cube and returns to the start location for further melting. Consequently, there are multiple reheating occurring within the spot melting scan strategy in a short period. Therefore, the return time should be additionally considered to maintain constant solidification conditions and achieve consistent microstructure across complex geometries.

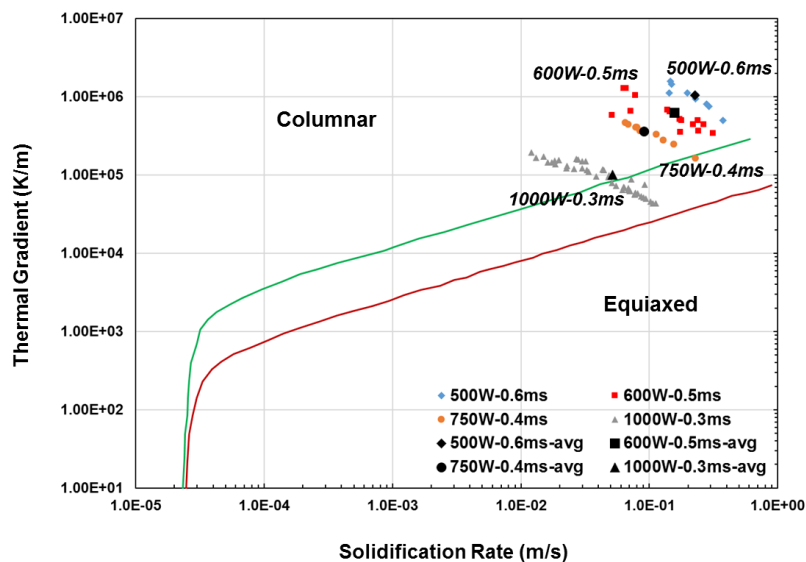


Figure 7 Effect of same energy density on solidification morphology

The beam return time at each case of 1 to 6 is shown in Table 3. The return time is calculated on the 20 mm x 20 mm layer. The result shows that the return time decreases with the decrease of spot time. It is obvious that beam spends less time at a location such that it results in shorter return time for the next heating cycle. It is important to note that solidification is a competition between heating and cooling. If the return time is shorter, the region heated in the earlier cycle does not have enough time to cool down such that reheating occurs before the melt pool completes the solidification. In other words, the area melting may not be achieved if the return time longer. Shorter return time helps to generate area melting but if it is too short, swelling could possibly happen due to shorter time available to diffuse the heat to the previously solidified layers and damage the build. Thermal diffusivity of the material and beam return time plays a significant role in achieving the balance between a successful build and failure due to swelling. Balance in power, beam on-time, and beam return-time is required to obtain the desired consistent microstructure. Thus, for a given material, a new factor ω is introduced considering power, spot time and return time together. The factor is given as below

$$\omega = \frac{Power}{Spot\ time \times Return\ time} \quad (5)$$

The calculated ω values in Table 3 captures the trend of G and R shown in Fig. 7. When the value of ω is small, the curve sits on the right-top region. As the value increases, the curve shifts to the left-bottom region. Equiaxed structure is observed in case 5 (Fig. 3) with the return time of 65.75 ms whereas columnar/mixed structure is observed for the case 4 (Fig. 7) with 78.9 ms return time. It seems that the return time for cube 4 is too long to produce the equiaxed structure. Thus, to keep constant heat accumulation over the layer, the return time for cube 4 should be recalculated based on the factor ω . For instance, the ω value of 73 W/ms² from the cube 5 is used to calculate a new return time for cube 4 to create equiaxed structure. Hence, the new return time, 45.66 ms, is recalculated for cube 4. A total number of spots corresponding to the return time is 152.2 spots (=45.66 ms/ 0.3 ms). The build dimension corresponding to 152.2 spots can be estimated based on scan strategy. For the beta scan strategy, the area of 16 mm x 16 mm contains 170 spots. For better accuracy, the spot time is recalculated due to the discrepancy in the number of spots (about 10% error = 170/152.2 spots). The calculated value of spot time is 0.27 ms (=45.66 ms /170 spots) for the area of 16 mm x 16 mm. Eventually, the optimal values of 1000W and 0.27 ms are generated for 16 mm x 16 mm cube.

Table 3 Beam return time at same energy

Case Number	Power (W)	Spot Time (ms)	Return Time (ms)	ω (W/ms ²)
1	500	0.60	157.80	5.28
2	600	0.50	134.50	8.92
3	750	0.40	105.20	17.82
4	1000	0.30	78.90	42.25
5	1200	0.25	65.75	73.00
6	1500	0.20	52.60	142.59

Figure 8 compares the shape of melt pool at different build size and resultant solidification morphology. The optimal parameters, 1000 W, and 0.27 ms, calculated from ω are used for the simulation with a dimension of 16 mm x 16 mm. Notice that the identical shape of area melting is achieved in Fig. 8(b). Also, the values of G and R from the small build sit in the same equiaxed region in Fig. 8(c). The build area is reduced by 36% but the energy into the build is lowered by 10%. It shows that additional parameters, return time and ω , should be considered when one selects process parameters to create same microstructure at different build size.

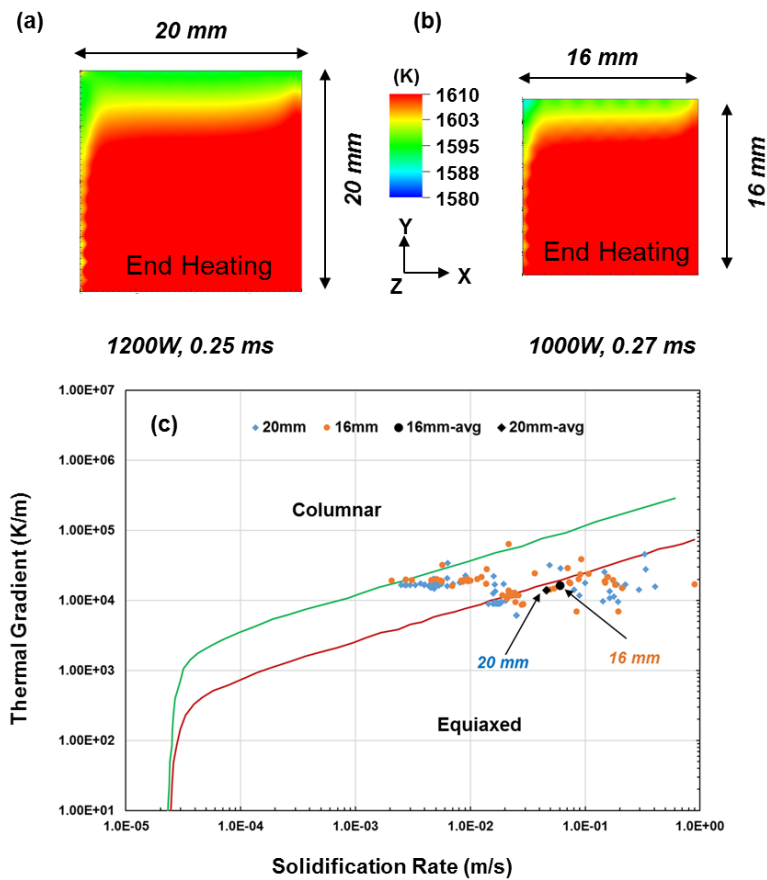


Figure 8 Identical melt pool shape at the different build size of (a) 20 mm by 20 mm and (b) 16 mm by 16 mm and (c) the predicted equiaxed microstructure on CET curve

4. Summary and Conclusion

In summary, the low-fidelity heat transfer model was developed to provide a quantitative understanding of the effect of process parameters on the thermal gradient G and solidification rate R . The model simulated approximately 10,000 melt spots filling the entire layer of the sample. Through the investigation of the simulation results, the following conclusion can be made:

- The low-fidelity heat transfer model makes a reasonable prediction of CET. The numerical results were validated with the corresponding experiments.
- Changing the scan strategy in β and γ build leads to different solidification morphology of equiaxed and columnar structure, respectively.
- The simulation shows that the G and R curve is moved even at the same energy density generated by a different set of power and spot time. It indicates that beam return time should be additionally considered to produce same microstructure.
 - A factor ω is introduced to include the effect of return time on top of the power and spot time. The calculated value of ω predicted well the trend of CET shift.
 - With optimal power and spot time recalculated based on ω , identical area melting and resultant solidification morphology is produced at the small build of 16 mm x 16 mm.
 - It concludes that, in addition to scan strategy, the build geometry also influences solidification microstructure. Appropriate modifications of process parameters should be made with respect to build geometry.

5. Acknowledgements

The research was sponsored by the US Department of Energy, Office of Energy Efficiency and Renewable Energy, Advanced Manufacturing Office under contract DE-AC05-00OR22725 with UT-Battelle, LLC.

6. References

- [1] R.R. Dehoff, M.M. Kirka, W.J. Sames, H. Bilheux, A.S. Tremsin, L.E. Lowe, S.S. Babu, Site specific control of crystallographic grain orientation through electron beam additive manufacturing, *Mater. Sci. Technol.*, 2015, 31, pp.931-938.
- [2] J. Raplee, A. Plotkowski, M.M. Kirka, R. Dinwiddie, A. Okello, R.R. Dehoff, S.S. Babu, Thermographic Microstructure Monitoring in Electron Beam Additive Manufacturing, *Sci. Rep.*, 2017, 7, pp.43554.
- [3] N. Raghavan, R. Dehoff, S. Pannala, S. Simunovic, M. Kirka, J. Turner, N. Carlson, S.S. Babu, Numerical modeling of heat-transfer and the influence of process parameters on tailoring the grain morphology of IN718 in electron beam additive manufacturing, *Acta Mater.*, 2016, 112, pp.303-314.
- [4] M. Gäumann, C. Bezencon, P. Canalis, W. Kurz, Single-crystal laser deposition of superalloys: processing–microstructure maps, *Acta Mater.*, 2001, 49, pp.1051-1062.

- [5] W. Kurz, B. Giovanola, R. Trivedi, Theory of microstructural development during rapid solidification, *Acta Metall.*, 1986, 34, pp.823-830.
- [6] W. Yan, W. Ge, Y. Qian, S. Lin, B. Zhou, G.J. Wagner, F. Lin, W.K. Liu, Multi-physics modeling of single/multiple-track defect mechanisms in electron beam selective melting, *Acta Mater.*, 2017.
- [7] A. Klassen, V.E. Forster, V. Juechter, C. Körner, Numerical simulation of multi-component evaporation during selective electron beam melting of TiAl, *J. Mater. Process. Technol.*, 2017, 247, pp.280-288.
- [8] Y. Lee, W. Zhang, Modeling of heat transfer, fluid flow and solidification microstructure of nickel-base superalloy fabricated by laser powder bed fusion, *Addit. Manuf.*, 2016, 12, pp.178-188.
- [9] S.A. Khairallah, A.T. Anderson, A. Rubenchik, W.E. King, Laser powder-bed fusion additive manufacturing: physics of complex melt flow and formation mechanisms of pores, spatter, and denudation zones, *Acta Mater.*, 2016, 108, pp.36-45.
- [10] M. Markl, R. Ammer, U. Rüdte, C. Körner, Numerical investigations on hatching process strategies for powder-bed-based additive manufacturing using an electron beam, *Int. J. Adv. Manuf. Tech.*, 2015, 78, pp.239-247.
- [11] A.J. Pinkerton, L. Li, Modelling the geometry of a moving laser melt pool and deposition track via energy and mass balances, *J. Phys. D: Appl. Phys.*, 2004, 37, pp.1885.
- [12] M. S. Alnaes, J. Blechta, J. Hake, A. Johansson, A.L. B. Kehlet, C. Richardson, J. Ring, M. E. Rognes, G.N. Wells, The FEniCS Project Version 1.5, *Archive of Numerical Software*, 2015, 3, doi: <http://dx.doi.org/10.11588/ans.2015.100.20553>.
- [13] B.E. Abali, Computational Reality, 1-ed., Springer, 2017.
- [14] H.P. Langtangen, A. Logg, Solving PDEs in Python, 1-ed., 2016.
- [15] K. Abderrazak, S. Bannour, H. Mhiri, G. Lepalec, M. Autric, Numerical and experimental study of molten pool formation during continuous laser welding of AZ91 magnesium alloy, *Comput. Mater. Sci.*, 2009, 44, pp.858-866.
- [16] A. Logg, G.N. Wells, DOLFIN: Automated finite element computing, *ACM Trans.Math. Softw.*, 2010, 37, p.20.
- [17] P. Prabhakar, W. Sames, R. Dehoff, S. Babu, Computational modeling of residual stress formation during the electron beam melting process for Inconel 718, *Addit. Manuf.*, 2015, 7, pp.83-91.
- [18] M.M. Kirka, Y. Lee, D.A. Greeley, A. Okello, M.J. Goin, M.T. Pearce, R.R. Dehoff, Strategy for Texture Management in Metals Additive Manufacturing, *JOM*, 2017, 69, pp.523-531.
- [19] K. Prashanth, S. Scudino, T. Maity, J. Das, J. Eckert, Is the energy density a reliable parameter for materials synthesis by selective laser melting?, *Mater. Res. Lett.*, 2017, pp.1-5.